Chapter 4
Functionalization of Graphene Nanoribbons

Haldun Sevinçli, Mehmet Topsakal, and Salim Ciraci

Abstract With the synthesis of a single atomic plane of graphite, namely, graphene honeycomb structure, a new perspective for carbon-based electronics is opened. The one-dimensional graphene nanoribbons (GNRs) have different band-gap values depending on their edge shape and width. In this contribution, we report our results showing that repeated heterostructures of GNRs of different widths form multiple quantum-well structures. The widths of the constituent parts as well as the bandgap, and also the magnetic ground state of the superlattices are modulated in direct space. We provide detailed analysis of these structures and show that superlattices with armchair edge shapes can be used as resonant tunneling devices and those with zigzag edge shape have unique features for spintronic applications. We also discuss another route of functionalizing 2D graphene, 1D GNR, and superlattices with 3d-transition metal (TM) atom adsorption.

4.1 Introduction

Carbon plays a unique role in nature by forming a number of very different structures. It is not only because it is capable of forming complex networks, which are fundamental to organic chemistry, but also due to the seldom properties of its zero-, one-, two-, and three-dimensional allotropes, which are subjects of solid state physics. Its 3D structures (diamond and graphite) have been known since ancient times, whereas the zero (fullerenes) and 1D (carbon nanotubes and linear atomic

S. Ciraci (✉)
Department of Physics, Bilkent University, 06800 Ankara, Turkey

UNAM, Institute of Materials Science and Nanotechnology, Bilkent University, 06800 Ankara, Turkey
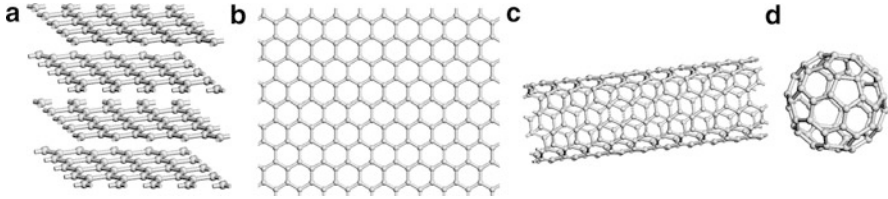e-mail: ciraci@fen.bilkent.edu.tr

Fig. 4.1 Graphitic carbon allotropes of three, two, one, and zero dimensions (**a–d**), respectively

chains) were discovered within the last 10–20 years. The experimental observation of 2D carbon (graphene) has been accomplished only recently [1].

Observation of truly 2D graphene made it necessary to reconsider the existing theories on low-dimensional crystals [2–4]. Despite earlier theories against the existence of perfect 2D crystals, a detailed analysis of the problem beyond the harmonic approximation has led to the conclusion that the interaction between bending and stretching long-wavelength phonons could, in principle, stabilize atomically thin membranes through their deformation in the third dimension. Analysis of the phonon dispersions within the quasi-harmonic approximation shows that 2D and 1D honeycomb structures of Si, Ge, and BN are also stable [5, 6].

The 2D honeycomb structure of graphene plays a crucial role for understanding other graphitic forms (Fig. 4.1), and the electronic properties of graphene are governed by the binding characters of its orbitals. A σ bond is formed between neighboring carbon atoms by sp^2 hybridization between one s-orbital and two p-orbitals. The remaining p-orbitals are perpendicular to the graphene plane and they form covalent bonds leading to a π-band.

Graphene is a zero bandgap semiconductor with linear dispersion of bands near the Fermi level. This particular dispersion gives rise to the lower energy excitations to behave as massless Dirac fermions with an effective speed of light v_F–10^6 m/s. Hence, at low energies, unusual properties of quantum electrodynamics are expected to be observed on graphene lattice. One of the interesting features of Dirac fermions is the deterministic (unit probability) transmission through tunneling barriers of arbitrary width and height when incident normally. This counterintuitive property of ultra-relativistic particles, known as Klein paradox, was previously attributed only to exotic phenomena such as black hole evaporation; now graphene serves as a basis to verify these [7].

Besides its unusual properties, graphene is a candidate for a large number of applications and has the potential to offer new concepts in materials research and fundamental science [8, 9]. A variety of methods have been proposed or demonstrated in order to functionalize graphene-based materials for new device applications [10–20] such as hydrogen storage media [10, 11], gas sensors [12], spin-valve devices [13–17], transistors [18,19], and resonant tunneling devices [20].

In this chapter, we present our work on functionalization of graphene nanoribbons (GNRs). The methods used are the empirical tight binding method and density functional theory (DFT) [29] (see Appendix A for details of DFT calculations).

Below, we first present a review of fundamental electronic and magnetic properties of graphene and GNRs, which will form a basis for the following sections, where we analyze the superlattice structures of armchair and zigzag GNRs. We also discuss the effects of adsorbed Ti atoms on the electronic and magnetic properties. We conclude this chapter with our findings.

4.2 Electronic and Magnetic Properties of 2D and 1D Graphene

4.2.1 Electrons in Honeycomb Lattice

The hexagonal lattice of graphene and its reciprocal lattice are shown in Fig. 4.2a and b. The lattice vectors are $a_1 = a(\sqrt{3}/2, 3/2)$ and $a_2 = a(-\sqrt{3}/2, 3/2)$ with $a = 1.42$ Å being the nearest neighbor distance. Correspondingly, the reciprocal lattice vectors are $b_1 = 2\pi/3a(\sqrt{3}, 1)$ and $b_2 = 2\pi/3a(-\sqrt{3}, 1)$. The corners of the first Brillouin zone, $K = 2\pi/3a(1/\sqrt{3}, 1)$ and $K' = 2\pi/3a(-1/\sqrt{3}, 1)$ are of particular importance for the physics of graphene. These points are called the Dirac points close to which the energy dispersion becomes linear as it will be discussed below.

The tight-binding Hamiltonian has the simple form

$$H_{\text{TB}} = -t \sum_{<i,j>\alpha\sigma} (c^+_{i\alpha\sigma} c_{j\alpha'\sigma} + H.c.),$$

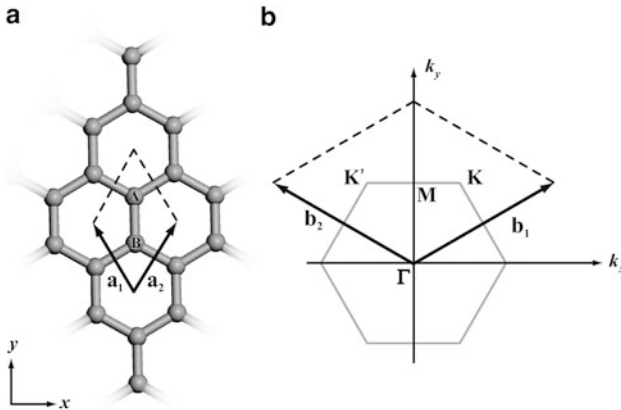**Fig. 4.2** (**a**) The lattice structure and the unit cell vectors of graphene. A and B atoms belong to different sublattices. (**b**) The corresponding Brillouin zone and the special k-points **r**, **M**, **K**, and **K′**
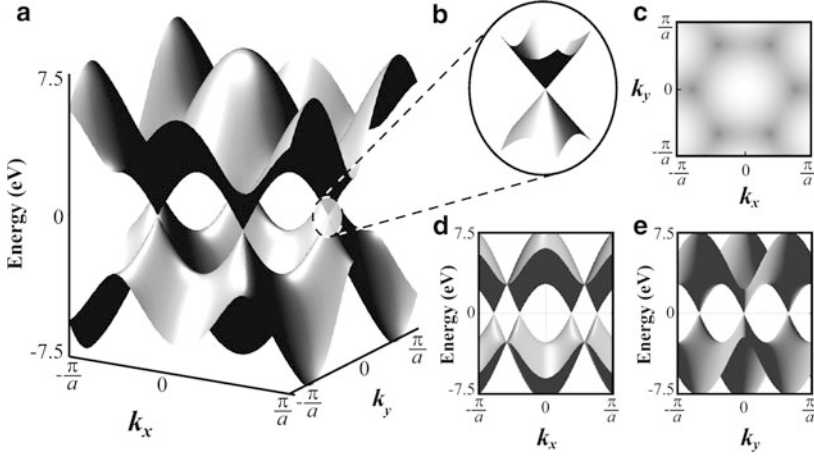
Fig. 4.3 The full band structure of graphene for $-\pi/a < kx$, $ky < \pi/a$ (**a**), and a zoom in of the band structure close to one of the Dirac points (**b**). (**c**) Two dimensional map of the conduction band. *Darker* regions indicate lower energy. (**d–e**) The full band structure from special view points corresponding to the band structures along the k_x- and k_y-directions. The k_x-direction can be named as the zigzag direction, and the k_y-direction as the armchair direction, and the ky-direction as the armchair direction in accordance with Fig. 4.2a (See also Figs. 4.5 and 4.6)

where $c^+_{i\,\alpha\,\sigma}(c_{i\,\alpha\,\sigma})$ creates (annihilates) an electron on site R_i with spin σ on the α sublattice, with α = A or B. The nearest neighbor ($\langle i, j \rangle$) hopping energy is $t \simeq 2.7$ eV [21]. The energy bands obtained from this Hamiltonian have the form

$$E_\pm k = \pm t \sqrt{3 + f(k)}$$

with

$$f(k) = 2\cos\left(\sqrt{3}k_x a\right) + 4\cos\left(\frac{\sqrt{3}}{2}k_x a\right)\cos\left(\frac{3}{2}k_y a\right),$$

where the plus sign applies to $\pi-$, and the minus sign to the π^*-bands. Evidently, the above bands satisfy electron-hole symmetry by being symmetric around the zero of the energy. The full band structure of graphene obtained from the tight-binding Hamiltonian is shown in Fig. 4.3a. In Fig. 4.3b a zoom-in of the band structure to one of the Dirac points is shown. Figure 4.3d and e shows the band structure from two special view points.

The energy dispersions can be expanded around K (or K') as $E_\pm \sim \pm h v_F |q|$ [22, 23]. Here, the Fermi velocity is $v_F = 3ta/2\hbar$ and $k = K + q$ with $|q| << |K|$, which enables us to write $f(k) = -3 + 9a^2(q_x^2 + q_y^2)/4$. In contrast to the usual case where $v = \sqrt{2E/m}$, the Fermi velocity of low-energy electrons of graphene does not depend on energy or momentum, which is the source of unusual effects.
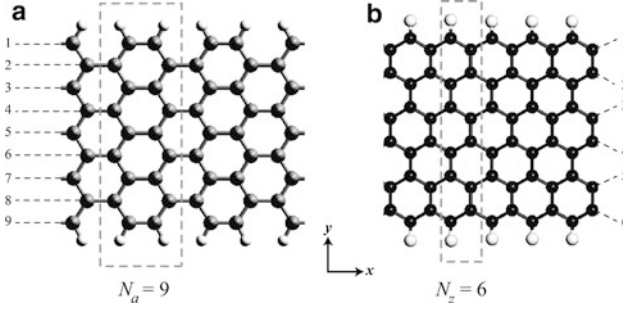
Fig. 4.4 Lattice structures of (**a**) AGNR(9) and (**b**) ZGNR(6). Unit cells of the structures are delineated, x-axis points the growth direction. The number $N_a = 9$ stands for the number of dimer lines while $N_z = 6$ stands for the number of zigzag chains along the x-direction

4.2.2 Electronic and Magnetic Properties of GNRs

The electronic structure and magnetic properties of GNRs are primarily determined by their edge shapes and their widths [24–28]. Their electronic structures also depend on whether the dangling bonds of the edge atoms are passivated or not. In this section, all the GNRs considered are those passivated with hydrogen. In Fig. 4.4a and b, the lattice structures and the unit cells of GNRs with armchair and zigzag edge shapes, respectively, are shown. Following the current literature, we denote GNRs having armchair edge shape with N_a dimer lines in the unit cell as AGNR(N_a), and those having zigzag edge shape with N_z zigzag chains in the unit cell as ZGNR(N_z).

DFT calculations show that AGNRs are direct bandgap semiconductors and their band gaps follow three curves depending on their width, namely, N_a [17]. For a given nonnegative integer n, $N_a = 3n + 1$ yields the highest bandgap whereas $N_a = 3n - 1$ yields the lowest, $N_a = 3n$ lying in between as shown in Fig. 4.5. As n increases, all three curves approach zero without crossing each other.

Although tight-binding calculations predict a zero bandgap for all ZGNRs [24] [e.g., Fig. 4.6a], DFT calculations show that all ZGNR are semiconductors and their bandgaps decrease monotonically with N_z, for $N_z > 4$ [45]. For all N_z values the highest valence band and the lowest conduction band give rise to a high density of states near the Fermi energy. These states are localized at the edges of the ZGNR and this give rise to an antiferromagnetic (AFM) ground state. Eventually, it is possible to express this magnetic transition by adding an on-site Hubbard term to the tight-binding Hamiltonian as

$$H_{\text{TB}} = -t \sum_{<i,j> \alpha \, \sigma} (c^+_{i \, \alpha \, \sigma} c_{j \, \alpha' \, \sigma} + H.c.) + U \sum_{i,\alpha} c^+_{i \, \alpha \, \sigma} c_{i \, \alpha \, \sigma} c^+_{i\alpha\sigma'} c_{i\alpha\sigma'}$$
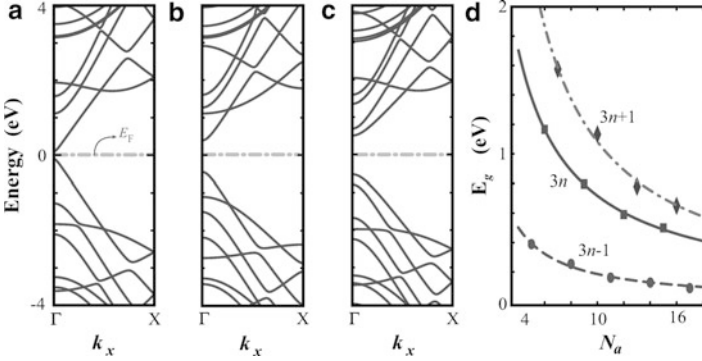
where is the on-site repulsion energy (26).

Fig. 4.5 Band structures of AGNRs belonging to different families: (**a**) $N_a = 3n - 1 = 8$, (**b**) $N_a = 3n = 9$, and (**c**) $N_a = 3n + 1 = 10$. (**d**) Bandgaps of the families as a function of N_a. Band structures are obtained using plane-wave DFT calculations, zero of the energy is set to E_F (Reproduced from Ref. [20])
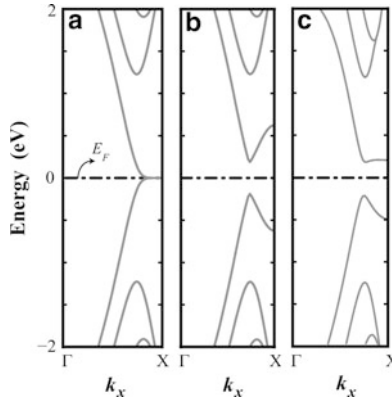

Fig. 4.6 Band structures of ZGNR(8) calculated by using three different methods: (**a**) tight-binding bands, (**b**) tight-binding bands including Hubbard correction within mean field approximation, where $U = 1.3\,\mathrm{eV}$, and (**c**) bands obtained from plane-wave DFT calculations. Zero of the energy axis is set to E_F

This Hamiltonian can be solved in the mean field approximation numerically. While the tight binding solution of the ZGNR Hamiltonian in the absence of Hubbard term yields a zero band gap semiconductor, upon inclusion of the Hubbard term ZGNR is found to be a direct band gap semiconductor (Fig. 4.6b) with edge states localized at the opposite edges having opposite spins. Such a magnetic solution of the Hubbard Hamiltonian for bipartite lattices was previously proved by Lieb [30], and these results are also verified by DFT calculations as shown in Fig. 4.6c.

4.3 Functionalization Through Superlattice Formation

The remarkable properties of GNRs discussed above, especially their bandgaps varying with their widths, suggest that the heterostructures formed by the segments of GNRs with different widths may have interesting electronic and magnetic properties. Here, the crucial issues to be addressed are how the electronic structure will be affected from the discontinuity of crystal potential at the junction; what the character of the band discontinuity and the resulting band alignment will be; and whether these discontinuities will result in confined states. In this section, we address these questions for both armchair and zigzag GNR superlattices (AGSL and ZGSL, respectively), and investigate the new functions which graphene-based materials can acquire upon size modulation.

4.3.1 Superlattices of Armchair Graphene Nanoribbons

Relative to the longitudinal axis in the armchair direction, one can distinguish three possible angles to make junctions with armchair or zigzag edge shapes as shown in Fig. 4.7a. A 60° angle gives rise to the armchair edge at the interface, whereas 30° and 90° angles result in zigzag edges. Some of the possible superlattice shapes are given in Fig. 4.7b–d.
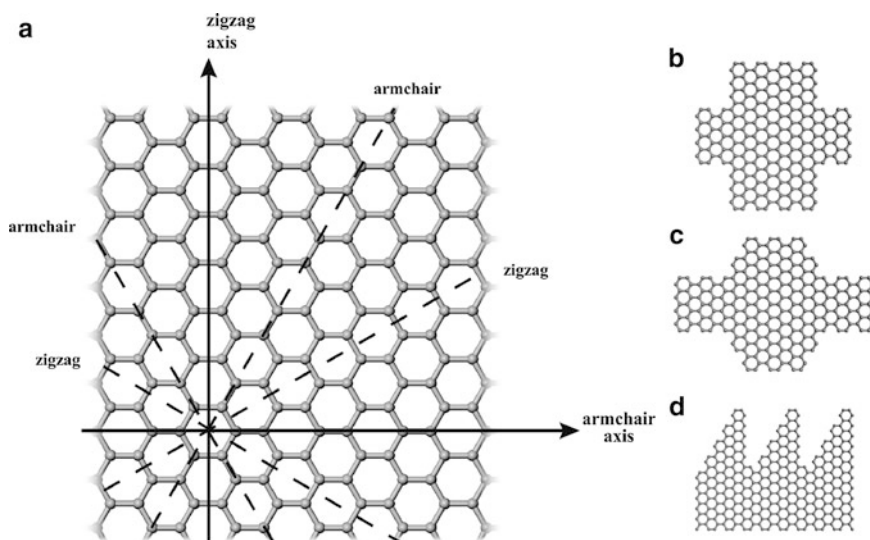

Fig. 4.7 (**a**) Crystallographic directions giving rise to armchair and zigzag edge shapes. Possible junction angles leading to armchair or zigzag edge shapes are indicated. 60° angle with the horizontal (armchair) axis results in armchair edge at the interface, whereas 30° and 90° give zigzag edges. Some of the possible superlattice shapes are shown, namely, (**b**) sharp rectangular, (**c**) smooth, (**d**) and sawtooth-like
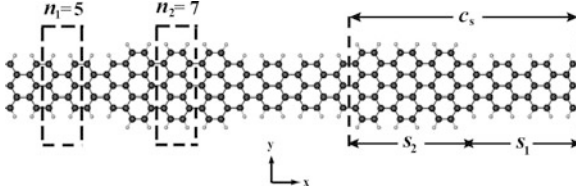
Fig. 4.8 Atomic structure of AGSL ($n_1 = 5$, $n_2 = 7$; $s_1 = 3$, $s_2 = 3$). The superlattice unit cell and primitive unit cell of each segment are delineated (Reproduced from Ref. [20])
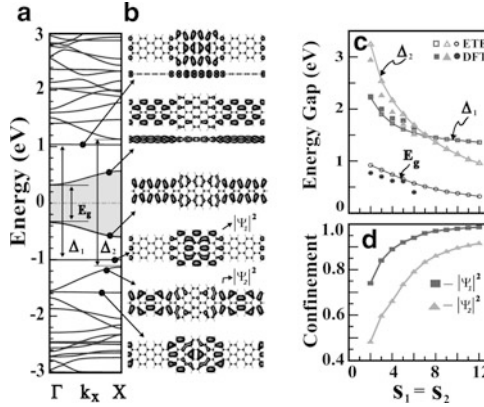

Fig. 4.9 Electronic structure of AGSL(5,7,3,3). (**a**) Band structure with flat bands corresponding to confined states. (**b**) Isosurface charge density of propagating and confined states. (**c**) Variation of various superlattice gaps with $s_1 = s_2$. (**d**) Confinement of states versus $s_1 = s_2$ calculated by ETB. All data except those in (**d**) are calculated by using first-principles method within DFT (Reproduced from Ref. [20])

In order to avoid mixed edge shapes, we focus on the junctions with smooth interfaces making 60° angle with the armchair axis. We first consider a superlattice AGSL(n_1,n_2;s_1,s_2) made by the segments of AGNR(n_1) and AGNR(n_2). Here, s_1 and s_2 specify the lengths (in terms of the number of GNR unit cells) of the segments having different widths. Figure 4.8 shows the superlattice AGSL(5,7;3,3). AGNR(5) and AGNR(7) are direct bandgap materials with bandgaps of 0.39 and 1.57 eV, respectively. The combined heterostructure with a symmetric junction has a bandgap of 0.65 eV. The band structure of segments and the supercell is shown in Fig. 4.9. Junction formation by these constituents gives rise to dramatic changes in the band structure of the superlattice. While the highest valance and the lowest conduction bands are dispersive, the bands below and above the dispersive ones are simply flat. The isosurface charge density plots distinguish the different characters of these bands. For example, as highest valence band states propagate across the superlattice, the states of the second (flat) band are confined to the wider part of AGSL(5,7;3,3) consisting of AGNR(7) segment. These flat band states are identified as *confined states*.

The confined states have been treated earlier in commensurate or pseudomorphic junctions of two different semiconductors, which form a periodically repeating superlattice structure. These superlattices have grown layer by layer and they form a sharp lattice matched interface [31–33]. Owing to the band discontinuities at the interface, they behave as a multiple quantum-well structure, obeying the effective mass theory. Generally, a particular state, which is propagating in one region (or segment), is confined if it cannot find a matching state in the adjacent region having the same energy. For a superlattice of small n_1 or n_2, spacings between energy levels are significant and, hence, localization of states in one of the regions is more frequent. This argument, which is relevant for superlattices of long constituent segments, may not be valid for short segments (i.e., small s_2 and s_2).

2D conduction band electrons (valence band holes), confined to the well, display a number of electronic and optical properties. In the present case, both the bandgap and the size (width) of the graphene ribbon are periodically modulated in direct space and the carriers are 1D. On the other hand, the atomic arrangement and lattice constants at both sides of the junction are identical; the heterocharacter concerns only the width of the ribbons at different sides. Electronic and transport properties of graphene multiple quantum-well structures can be controlled by a number of structural parameters. In addition to n_1, n_2, s_1, s_2, symmetry of the junction, $\Delta n = n_2 - n_1$, even–odd disparity of $n_1/2$ and $n_2/2$, type of the interface between two different ribbons and the shape of the superlattice (namely sharp rectangular or smooth wavy) influence the properties. As shown in Fig. 4.10, superlattice bandgaps decrease as s_1 increases from 3 to 8. This is a clear evidence for quantum size effect. In terms of the weight of the states in the segment s_2, i.e., $\int_{s_2} |\Psi(r)|^2 dr$, we see that the confinement of states increases with increasing s_1; but it disappears for $s_1 = s_2 = 1$. Confinement increases with increasing $s_1 = s_2$, and hence with increasing barrier width, since the penetration of states into the barrier decreases). For example, AGSL(5,7;s_1,s_2) has E_g = 0.66, 0.48, 0.38, 0.32, 0.27 eV for $s_2 = 3$ and s_1 = 3, 4, 5, 6, 7, respectively. Conversely, E_g = 0.72, 079, 0.83, 0.84 eV for $s_1 = 3$ and s_2 = 4, 5, 6, 7, respectively. On the other hand, the energy of the flat-band states confined to s_2 and their weight are practically independent of s_1.

We also investigate the effects of changing n_1 from 7 to 9. Two nanoribbons containing 10 and 18 carbon atoms in their unit cell are merged. Variation of $\Delta n = n_1 - n_2$ results in a wide variety of electronic structures. For example, in contrast to AGSL(5,7;3,3), the highest valence and lowest conduction bands of AGSL(5,9;3,3) are flat bands with E_g = 0.70 eV; dispersive bands occur as second valence and conduction band, having a gap of 1.18 eV between them. Since the first valence and conduction bands are confined in a wider region of the structure, this ribbon can act as a resonant tunneling double barrier (RTDB) device. The narrow regions act as a barrier and wider region as a quantum well. We have complete confinement of charges for some of states in the wider region. On the other hand, the states that are mostly confined in narrower region can penetrate to the wider regions. The variation of s_1 for AGSL(5,9;s_1,s_2) family has similar consequences to the AGSL(5,7;s_1,s_2). Again, we see that the confinement of states increase with increasing s_1. As shown in Fig. 4.11a–c superlattice bandgaps decrease as s_1

Fig. 4.10 The effect of the variation of length of the narrower region s_1 of AGSL (5,7; s1,3) from $s_1 = 3$–8. Note that the narrower region is acting like a barrier for the confined state. (**a**) Atomic structure and superlattice unit cell. (**b**) The variation of band structures. (**c**) The numerical values for energy gaps E_g, Δ_1, and Δ_2. E_g is the actual bandgap of the structure, which comes from a dispersive state. Δ_1 is the bandgap of highest localized state while Δ_2 is the bandgap for the next dispersive state. The energy of the flat-band states related to Δ_1 is confined to s_2 and their weights are practically independent of s_1. Calculations are carried out by using first-principles plane-wave methods within DFT (see Appendix A) (Reproduced from Ref. [20])
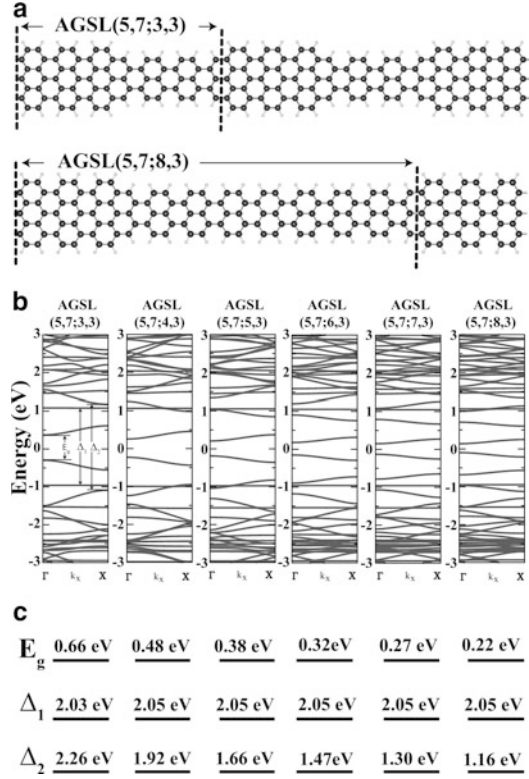
increase from 3 to 7. On the other hand, the energy of the flat-band states confined to s_2 and their weight are practically independent of s_1. As shown in Fig. 4.11d–f, the band gaps of localized conductance and valence states decrease with the increase in s_2. These findings reveal that charge confinement in size-modulated GNRs is closely related with the structural parameters of heterostructure.

In Fig. 4.12, we demonstrate that the confined states can occur not only in narrow (small n_1 and n_2) but also in wide superlattices having significant modulation of the width. The above trends corresponding to small n_1 and n_2 become even more interesting when n_1 and n_2 increase. The electronic band structure of AGSL(n_1,n_2;s_1,s_2) with $n_1 = 21$ or 41, but $n_2 > n_1$ and $s_1 = s_2 > 3$ calculated using ETB method shows that for small Δn, confinement is weak and bands are dispersive, but confinement increases as Δn increases. Interestingly, E_g of AGSL($n_1 = 21, n_2; 3, 3$) is, respectively, 0.46, 0.12, 0.49, and 0.04 eV for $n_2 = 23$, 25, 27, and 29. In ETB method used here, the Bloch states having band index 1 and wave vector k are expressed in terms of the linear combination of the orthonormalized Bloch sums $\chi_i(k, r)$ constructed for each atomic orbital p_z localized at different carbon atoms, i, with the proper phase of k, namely, $\Psi_l(k, r) = \sum_i a_{i,l}(k)\chi_i(k, r)$. Accordingly, the contribution of the orbital at site
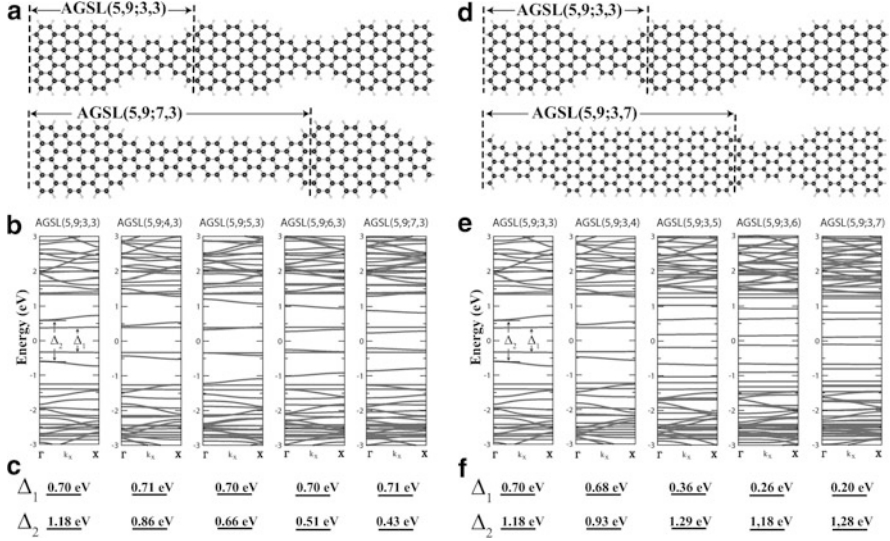
Fig. 4.11 Variation of energy band structure with superlattice parameters for AGSL(5,9,s_1,s_2) is investigated. $s_2 = 3$ is kept fixed while s_1 is varied from 3 to 7 (**a–c**), and then $s_1 = 3$ is kept fixed while s_2 is varied from 3 to 7 (**d–f**). Highest valence and lowest conduction bands of AGSL(5,9;3,3) are confined at the wider region. So their energies are practically insensitive to the length s_2 of the narrow region (**b**). But the spatial extend of the wave functions of these states influence their energies so that the band gap closes as s_2 is increased (**e**). Calculations have been performed using DFT method (see Appendix A).

i to the normalized charge density of $\Psi_l(k, r)$ is given by $\rho_i = \left| \sum_l a_{i,l}(k) \right|^2$. In Fig. 4.12, ρ_i is scaled with the radius of circles located at atomic site i.

The electronic properties are also strongly dependent on whether the geometry of the superlattice is symmetric (having a reflection symmetry with respect to the superlattice axis along the x-direction) or saddle (one side is straight, other side is periodically carved), all having the same Δn. While the saddle structure of AGSL(5,9;3,3) has the largest direct gap between dispersive conduction and valence bands, its symmetric structure has the smallest gap, but with the largest number of confined states. Horn-like smooth connection between wide and narrow segments (where the ribbon is carved from both sides smoothly and symmetrically) may give rise to adiabatic electron transport and focused electron emission [34].

4.3.1.1 Resonant Tunneling Double Barrier Device

In this section, we focus on a finite segment (flake) of GNR and calculate its transport properties. In accordance with the results of the previous section, we investigate the effect of confinement on transport properties upon modulation of the
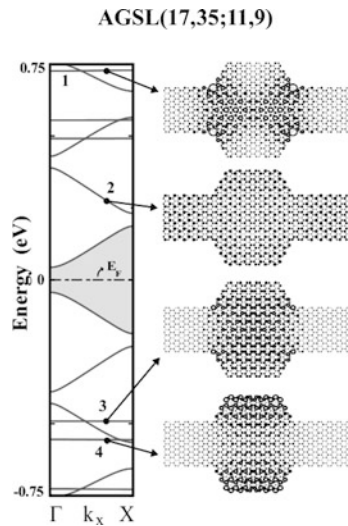
AGSL(17,35;11,9)

Fig. 4.12 Energy band structure of the AGSL(17,35;11,9) superlattice and the charge densities of selected bands. As seen clearly, states associated with flat bands 1, 3, and 4 are confined but the state with dispersive band indicated by 2 is propagating. Calculations have been performed using ETB method (Reproduced from Ref. [20])
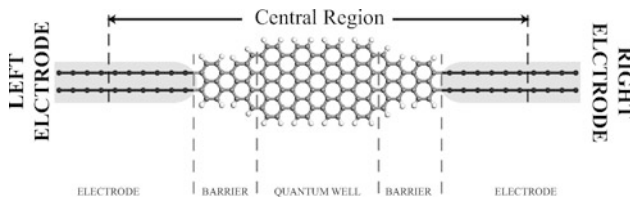

Fig. 4.13 Resonant tunneling double barrier device consisting of AGNR(5) and AGNR(9) segments. Parts of electrodes are included at both sides of AGNR segment as parts of the central device (Reproduced from Ref. [20])

ribbon width. We consider a finite armchair graphene nanoribbon with AGNR(5) and AGNR(9) as constituent parts having a total length of 8 unit cells, as shown in Fig. 4.13. Such a device is relevant for applications and uses the highest occupied molecular orbitals (HOMO) and lowest unoccupied molecular orbitals (LUMO) confined in the wide region.

Recently, patterning of GNRs [35], and also GNRs with varying widths [36, 37] are achieved, and it is shown experimentally that transport through GNRs is primarily influenced by the boundary shape [35]. These experiments reveal the importance of charge confinement effects on the conductance. Moreover, a suppression of conductance of GNRs by Coulomb blockade due to formation of multiple quantum dots in series, which are likely to form during the etching process, is also reported [37]. These facts support our idea that construction of a double
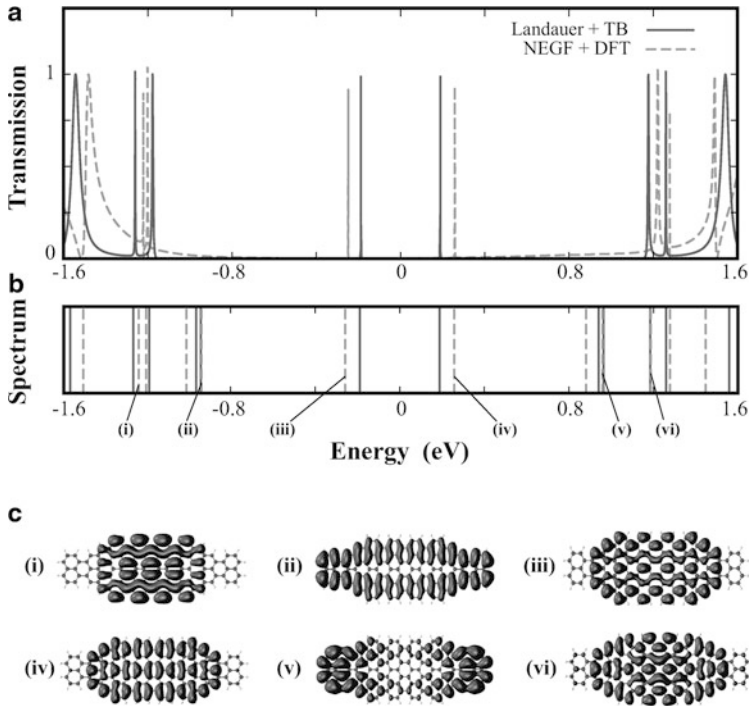
Fig. 4.14 (**a**) Transmission coefficient versus energy calculated under zero bias. Zero of the energy axis is set to the Fermi level. *Solid* curve stands for the DFT-based calculation whereas the *dashed* curve represents the ETB-based result within Landauer approach. (**b**) The energy spectrum of the uncoupled AGNR segment. (**c**) Charge densities of selected energy levels of the uncoupled AGNR segment indicating confined versus extended states (Reproduced from Ref. [20])

barrier device by modulating the width of a nanoribbon is realizable experimentally. For our quantum transport calculations, we consider generic metallic electrodes of two widely separated (weakly coupled) monatomic carbon chains. Carbon chains are known to have high cohesive energy and axial strength, and exhibit stability even at high temperatures [42]. Because of their flexibility and reactivity, carbon chains are suitable for structural and chemical functionalizations, and they are good metals with two quantum conductance channels, which make 4 units of quantum conductance at the Fermi level for the electrodes that we consider. Six principal layers of electrodes are included at both sides of resonant tunneling double barrier (RTDB) as parts of the central device. Metallic electrodes make perfect contacts with the central RTDB device. The transmission coefficient T reflects the combined electronic structure of central RTDB device, electrodes, and their contacts as shown in Fig. 4.14a.

The HOMO, LUMO and other confined states are identified through the energy level diagram [see Fig. 4.14b] and the isosurface charge density plots, obtained from plane wave *ab initio* calculations [see Fig. 4.14c]. The confined states give

rise to sharp peaks originating from resonant tunneling effect. States extending to the whole RTDB are coupled with the states of electrodes, and they are shifted and contributed broader structures in the transmission curve.

The resonant tunneling effect is not affected by the width of the barrier regions [namely, narrow AGNR(5) segments in Fig. 4.13a], considerably. The confined LUMO and HOMO states are weakly sensitive to the length of the barriers. This feature of confined states can also be observed from the energies of confined states (flat bands) of Fig. 4.11; for tunneling transport, wider barriers mean exponentially lower coupling between the quantum well region and the electrodes, which result in even sharper peaks at approximately the same energies.

4.3.2 Superlattices of Zigzag Graphene Nanoribbons

In this section, first-principles plane wave calculations [50] within DFT [29] using projector augmented wave (PAW) potentials [47] are performed (see Appendix A) to show that periodically repeated junctions of segments of zigzag ribbons with different widths can form stable superlattice structures. The energy bandgap and magnetic state of the superlattice are modulated in the real space. Edge states with spin polarization can be confined in alternating quantum wells occurring in different segments of ribbons. Even more remarkable is that the AFM ground state can be changed to ferrimagnetic (FRM) one in asymmetric junctions.

Zigzag graphene ribbons, i.e., ZGNR(N_z) with N_z zigzag chains in its unit cell, are characterized by the states at both edges of ribbon with opposite spin polarization [24]. These edge states attribute an AFM character (see Sect. 4.2). Under applied electric field the ribbon can become half-metallic [16].

We consider segments of two zigzag ribbons of different widths and different lengths, namely ZGNR(N_{z1}) and ZGNR(N_{z2}), which can make superlattice structures [32] with atomically perfect and periodically repeating junctions. Normally, the superlattice geometry can be generated by periodically carving small pieces from one or both edges of the nanoribbons [43]. Typical superlattices and their structural parameters are schematically described in Fig. 4.15. ZGNR(N_{z1})/ZGNR(N_{z2}) superlattices can be viewed as if a thin slab with periodically modulated width in the xy-plane. The electronic potential in this slab is lower ($V < 0$) than outside vacuum ($V = 0$). Normally, states in this thin potential slab propagate along the x-axis; but the propagation of specific states in ZGNR(N_{z2}) is hindered by the potential barrier above and below the narrow segment, ZGNR(N_{z1}). Eventually, these states are confined to the wide segments, and in certain cases also to the narrow segments. Here, the confinement of the states has occurred due to the geometry of the system. Defining the confinement in a segment i as $\int_i |\Psi(r)|^2 dr$, the sharper the interface between ZGNR(N_{z1}) and ZGNR(N_{z2}) the stronger becomes the confinement.
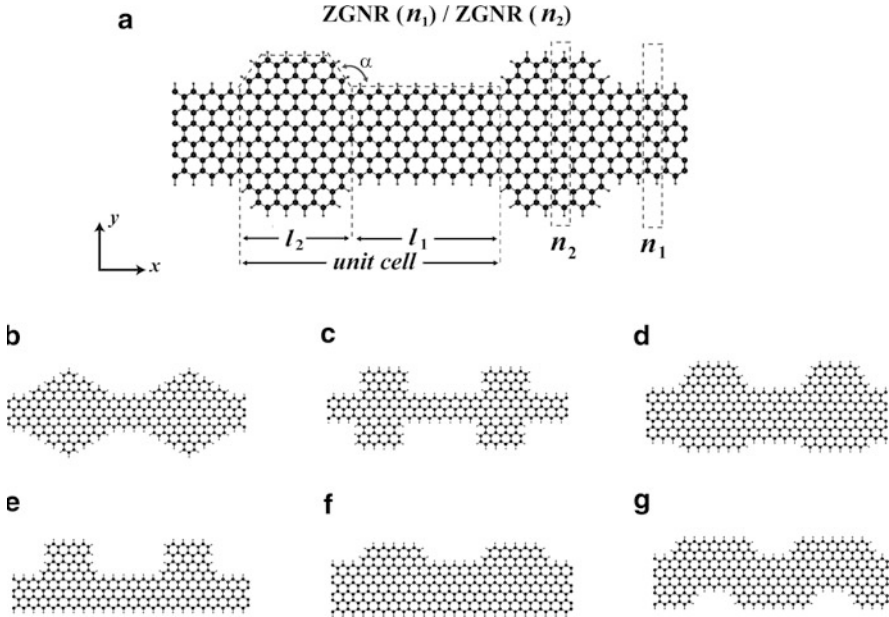
Fig. 4.15 Typical superlattice structures of zigzag graphene ribbons, ZGNR(N_{z1})/ZGNR(N_{z2}). N_{z1} and N_{z2} are the number of zigzag chains in the longitudinal direction; l_1 and l_2 are lengths of alternating ZGNR segments in numbers of hexagons along the superlattice axis. a is the angle between the x-axis and the edge of the intermediate region joining ZGNR(N_{z1}) to ZGNR(N_{z2}). $a = 120°$ or $90°$ for (**b–g**). *Dark-large balls* and *small-light balls* indicate carbon and hydrogen atoms, respectively (Reproduced from Ref. [14])

We show a symmetric superlattice ZGNR(4)/ZGNR(8) in Fig. 4.16. Spin-up and spin-down edge states at the top of the valence band of AFM superlattice are confined to the opposite edges of the narrow segments of the superlattice. Normal flat band states near -1.2 eV are confined to the wide segments of ZGNR(8). The energy band structure of the superlattice is dramatically different from those of the constituent nanoribbons. If the lengths of the segments are sufficiently large, these segments display the bandgap of the corresponding infinite nanoribbon in real space. The total magnetic moment of spin-up and spin-down edge states is zero in each segment, but the magnetic moment due to each edge state is different in adjacent segments. As a result, the superlattice remains to be an AFM semiconductor, but the magnitudes of the magnetic moments of the edge states are modulated along the x-axis. The coupling between the magnetic moments localized in the neighboring segments is calculated to be 15 meV per unit cell. The modulation of magnetic moments can be controlled by the geometry of the superlattice. For example, as shown in Fig. 4.16d, the magnetic moments of the atoms in the wide segment are practically zero and, hence, the superlattice is composed of AFM and nonmagnetic (NM) segments. However, as $l_2 \rightarrow 10$ the magnetic moments of the edge atoms at the wide segment become significant.
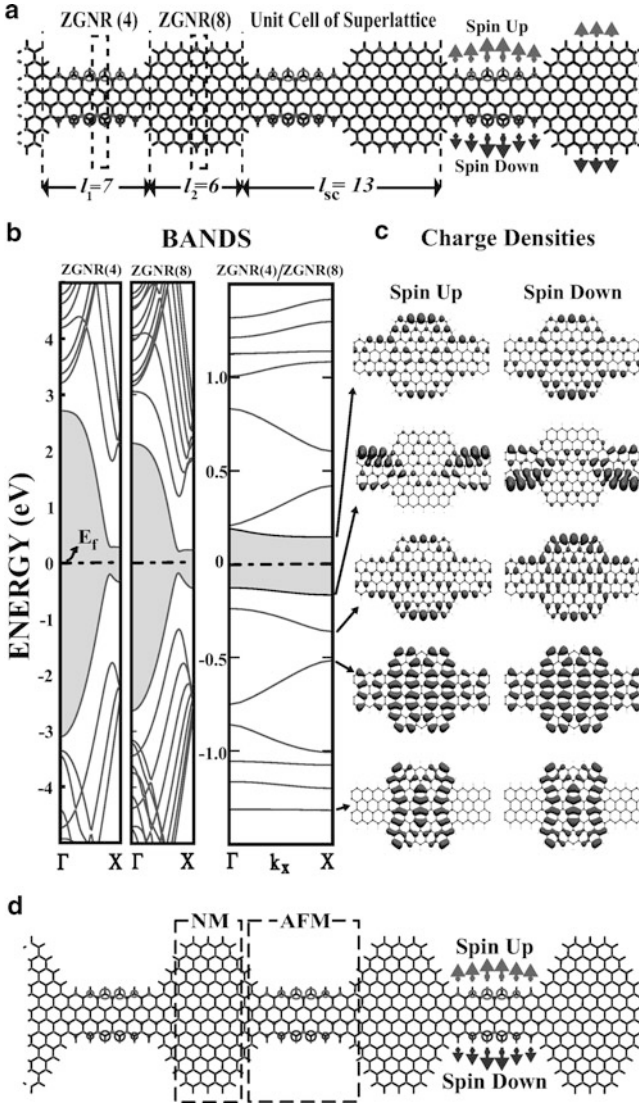
Fig. 4.16 (**a**) A schematic description of the symmetric ZGNR(4)/ZGNR(8) superlattice with relevant structural parameters. Magnetic moments on the atoms are shown in the *left* cell by *dark* and *light circles* and *arrows* for positive and negative values. l_{sc} is the length of the superlattice unit cells in terms of number of hexagons along the *x*-axis. (**b**) Energy band structures of antiferromagnetic (AFM) ZGNR(4), ZGNR(8) ribbons and AFM ZGNR(4)/ZGNR(8) superlattice. (**c**) Charge density isosurfaces of specific superlattice states. Zero of the energy is set to Fermi level, E_F. The gap between conduction and valence bands are shaded. (**d**) A specific form of superlattice ZGNR(4)/ZGNR(12) with alternating AFM and nonmagnetic (NM) segments in real space. Calculations have been performed using DFT method (see Appendix A) (Reproduced from Ref. [14])
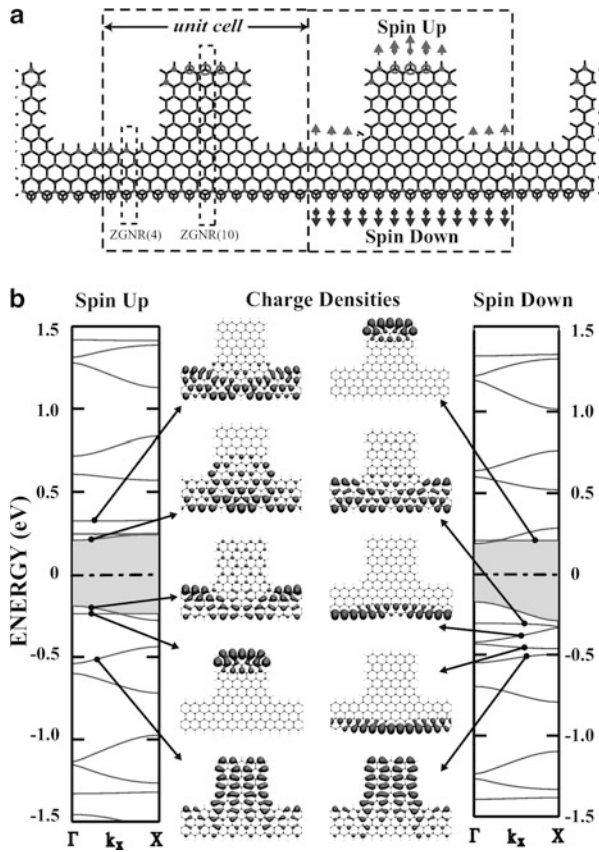
Fig. 4.17 (**a**) A schematic description of an asymmetric ZGNR(4)/ZGNR(10) superlattice. Total majority and minority spins shown by *light* and *dark circles* (for spin-up and spin-down, respectively) attribute a ferrimagnetic (FRM) behavior. (**b**) Energy band structure of the FRM semiconductor and charge density isosurfaces of specific propagating and confined states of different spin polarization. Calculations have been performed using DFT method (see Appendix A) (Reproduced from Ref. [14])

Asymmetric superlattice structure shown in Fig. 4.17 is even more interesting. While the spin-down states remain propagating at the flat edge of the superlattice, spin-up states are confined predominantly at the opposite edge of the wide segments. Confinement of states and absence of reflection symmetry breaks the symmetry between spin-up and spin-down edge states. Hence, the superlattice formation ends up with a FRM semiconductor having different bandgaps for different spin states. In agreement with Lieb's theorem [30, 44], the net magnetic moment calculated to be 2 is equal to the difference of the number of atoms belonging to different sublattices. Flat bands at the edges of spin-up valence band and spin-down conduction band are of particular interest. The spin states of these bands are confined to the discontinuous

edges of the wide segment, which behave as a quantum well. Since a device consisting of a finite size superlattice connected to two electrodes from both ends has high conductance for one spin direction, but low conductance for the opposite one, it operates as a spin valve. Moreover, spin-down electrons injected to this device are trapped in one of the quantum wells generated in a wide segment. As a final remark, we note that the DFT method underestimates the bandgaps found in this work [45]. However, this situation does not affect our conclusions in any essential manner.

4.4 Functionalization Through TM-Atom Doping

Another route in functionalization of graphene-based materials is adsorbing TM atoms on them. In this section, we present results of *ab initio* total energy DFT calculations concerning the equilibrium geometries, electronic and magnetic properties of 3d TM atom adsorbed graphene, AGNR, and AGSL.

We first investigate the binding energies and minimum energy geometries of either (2×2) or (4×4) unit cell of graphene when a Ti, Co, Fe, Cr, or Mn atom adsorbed. Three different sites are considered for adsorption to a (2×2) unit cell which are the hollow site (H) above the center of a hexagon, the bridge site (B) over a carbon–carbon bond, and the top site (T) over a carbon atom. H-site is the minimum energy site for Ti, Co, Fe, and Mn, whereas Cr prefers the B-site. We check the magnetic state of the structure by doubling the previous geometry in both lattice vector directions and setting the initial magnetic state as AFM. The minimum energy geometries, magnetic states, binding energies, and total magnetic moments of adsorption to (2×2) graphene cell are given in Table 4.1. Comparison of binding energies of adsorption on (2×2) cell with that of (4×4) cells indicates that bindings to the smaller one are weaker. This is because TM–TM coupling is more significant in (2×2) case and this coupling energy is subtracted from the binding energy (see Appendix A).

We calculate the charge accumulation for majority ($\uparrow$) and minority ($\downarrow$) spins for Ti adsorption on (4×4) cell as $\Delta\rho_{\uparrow(\downarrow)} = \rho_{\uparrow(\downarrow)}$ [graphene + Ti] $-\rho_{\uparrow(\downarrow)}$[graphene] −

Table 4.1 Minimum energy adsorption sites and magnetic states (either ferromagnetic (FM) or antiferromagnetic(AFM)) for single-sided adsorption of one TM atom adsorbed per (2×2) cell

	Ti	Co	Fe	Cr	Mn
	H AFM	H FM	H FM	B AFM	H AFM
E_b(eV)	1.58	1.20	0.66	0.18	0.10
	(1.95)	(1.27)	(1.02)	(0.20)	(0.17)
$\mu_{tot}(\mu B)$	0.0	1.31	3.02	0.0	0.00
d (Å)	2.32	2.12	2.21	2.39	2.47

The binding energies (E_b), the total magnetic moments μ_{tot}, and the distances to the nearest C atom (d) are also listed. The binding energy of a single TM atom adsorbed on a (4×4) cell is given in parentheses for the sake of comparison
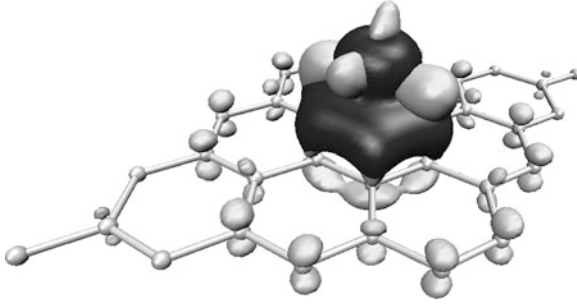
Fig. 4.18 Spin resolved charge accumulation (i.e. $\Delta\rho_{\uparrow(\downarrow)} > 0$) obtained from the charge density difference calculation for one Ti atom adsorbed to each (4×4) cell of graphene (see the text). *Dark* and *light* regions indicate the isosurfaces of majority and minority spin states, respectively. Calculations have been performed using DFT method (see Appendix A) (Reproduced from Ref. [46])

$\rho_{\uparrow(\downarrow)}$ [Ti]. Here $\rho_{\uparrow(\downarrow)}$ [graphene+Ti] is the total charge of the majority and minority spin states of one Ti atom adsorbed to each (4×4) cell of graphene. $\rho_{\uparrow(\downarrow)}$ [graphene] and $\rho_{\uparrow(\downarrow)}$ [Ti] are the charge densities of noninteracting bare graphene and Ti atom having the same positions as in the case of graphene and adsorbed Ti. The accumulation of spin-dependent charge densities due to adsorption are shown with the isosurface plot in Fig. 4.18. An increase in the majority spin density between graphene and Ti is accompanied with a net increase in minority spin density on Ti. The difference in majority and minority spin densities demonstrate the induced magnetization on $2p_z$ orbitals of the carbon atoms.

We also examine the variation of electronic and magnetic properties of TM-adsorbed AGNR's with different widths. We define the TM atom coverage θ as the number of TM atoms per unit cell and study the cases with $\theta = 1$ and 2. In the $\theta = 1$ case, we examine all the hollow sites for adsorption for AGNR's with $N_a = 4, 5, 6, 7, 8,$ and 9. For all TM species and all N_a edge, hollow site is found to have the minimum energy. Transition state analysis for the species with the strongest binding is given in Fig. 4.19. The energy barrier for a Ti atom to hop from the middle hexagon of a AGNR(7) unit cell to the edge hexagon is 0.48 eV, whereas the barrier height is 0.97 eV in the reverse direction [see Fig. 4.19c] These results suggest that the diffusion of Ti atoms to form clusters is hindered by a significant energy barrier. We further examine the TM-adsorbed AGNRs by considering $\theta = 2$ case. We keep the first TM atom at the hollow of the edge hexagon and check all the possible adsorption sites for the second TM atom. We calculate three cases with $N_a = 4, 5,$ and 6 to sample the three families of AGNR band structures. The energy is lowered by TM–TM interaction, so the second TM atom prefers the hexagon, which is closest to both the first TM atom and the ribbon edge [see Fig. 4.20a]. Consequently, a zigzag chain of TM atoms is formed at the edge of the AGNR. Such a chain formation either metallizes the system or it gives to half-metallicity. For example, zigzag chain of Fe on AGNR(5) is half-metallic with an energy gap
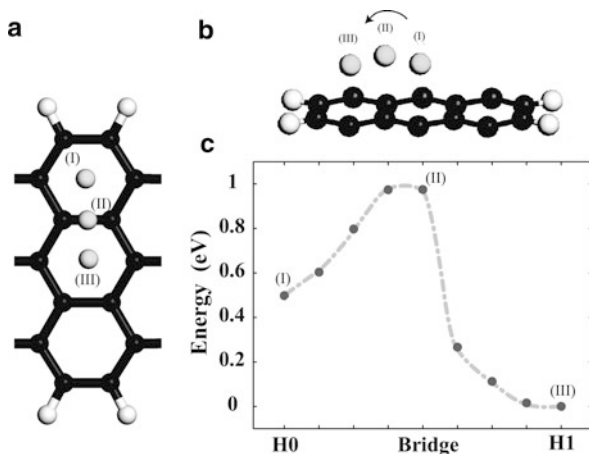
Fig. 4.19 Transition state analysis of Ti adsorbed on AGNR(7) between H0 and H1 sites above the bridge site. (**a**) *Top view* of three adsorption sites of Ti on AGNR(7) from H0 to H1, i.e., H0 bridge and H1 sites are shown. (**b**) *Side view* for these three adsorption sites. Adsorption to the C–C bridge gives the farthest position to the AGNR plane. (**c**) Total energy per unit cell for Ti adsorption on the path from H0 to H1 as explained in the text. Calculations have been performed using DFT method (see Appendix A) (Reproduced from Ref. [46])
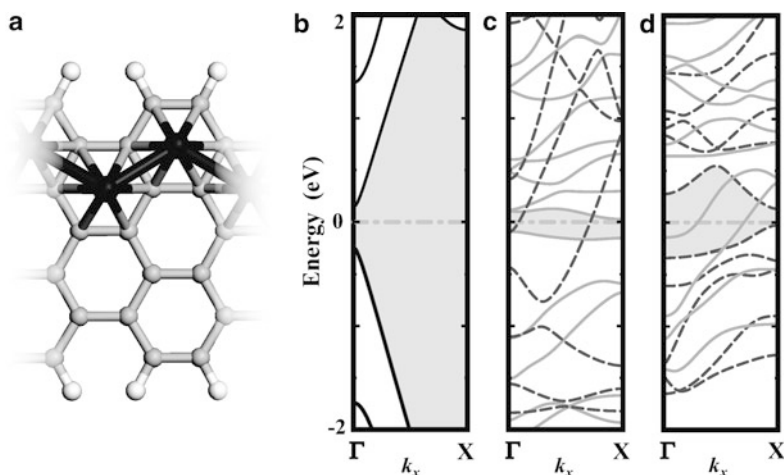

Fig. 4.20 Zigzag chains are formed at the AGNR edge for $\theta = 2$ coverage (**a**). Band structures of (**b**) bare AGNR(5) and $\theta = 2$ coverage of AGNR(5) (**c**) with Fe, and (**d**) with Ti. Fermi Energy is set to zero. In (**c**) and (**d**), *dark-dashed curves* are the bands with majority spin, and *light-solid curves* are the bands of the minority spin. Fe adsorption opens a gap of 0.10 eV for the minority spin while the majority spin is metallic. Adsorption of Ti makes the minority spin metallic while the majority spin has an energy gap of 0.16 eV at the Fermi energy (Reproduced from Ref. [46])
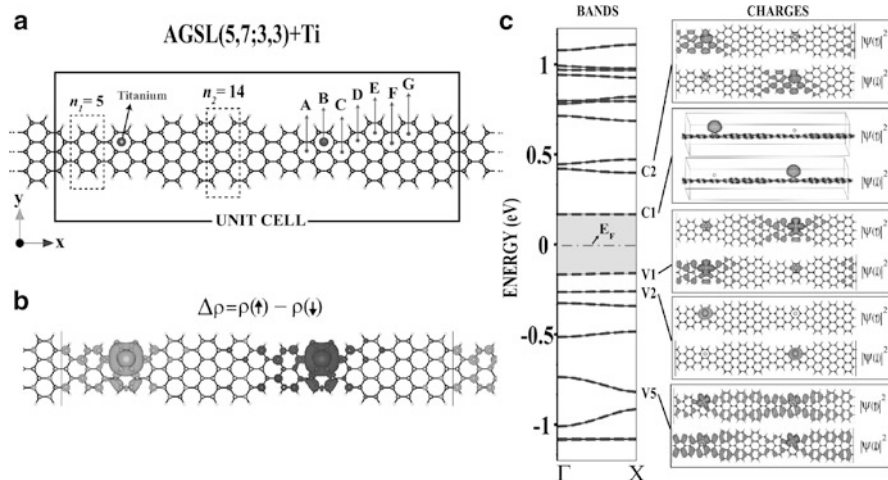
Fig. 4.21 (**a**) Atomic configuration of Ti-adsorbed AGSL(5,7;3,3). The primitive unit cells are delineated by *dashed lines*. The possible adsorption sites are labeled by letters A–G. (**b**) Isosurface of difference charge density of spin-up and spin-down states, $\Delta\rho = \rho(\uparrow) - \rho(\downarrow)$. *Light* regions correspond to positive and *dark* regions correspond to negative difference. (**c**) Energy band structure and isosurface charge density of selected spin states. $\Psi(\uparrow)$ is for spin-up component and $\Psi(\downarrow)$ is for spin-down component

of 0.10 eV for minority spin electrons [Fig. 4.20c]. Similarly, Ti zigzag chains at the edges of AGNR(4) and AgNR(5) are half-metallic with energy gaps of 0.05 and 0.16 eV for the majority spin electrons [Fig. 4.20d].

These results show that the ribbon width and the interaction of the TM atom with ribbon edge play important roles in the electronic properties of GNRs. We furthermore investigated Ti atom adsorption on armchair graphene superlattice structures that are studied in Section 4.3. For Ti adsorption, we have chosen AGSL(5,7;3,3) superlattice whose atomic configuration is presented in Fig. 4.8. All the hexagons from (A)–(G) in Fig. 4.21a has been checked and we found that (B) site corresponds to the minimum energy configuration. Ti atoms prefer to stay in narrower parts of the superlattice. This result is predictable when our previous results about adsorption on AGNR are analyzed. Binding energy is higher for adsorption on AGNR(5) compared to adsorption on AGNR(7) [46]. The magnetic configuration of two Ti atoms was investigated and we found that antiferromagnetic arrangement of the spins of two Ti atoms is 8 meV, energetically more favorable than ferromagnetic arrangement. The exchange energy is calculated from the difference of E_{AFM} (antiferromagnetic state) and E_{FM} (ferromagnetic state) and is related to J in the Heisenberg Hamiltonian. The relatively small exchange energy shows that indirect exchange coupling between Ti atoms is small when mediated through superlattice structures of graphene ribbons. Isosurface plots of difference in charge density between up-spin and down-spin states, $\Delta\rho = \rho(\uparrow) - \rho(\downarrow)$ in Fig. 4.21b clearly reveals the antiferromagnetism in the system.

The electronic structure of AGSL(5,7;3,3) in Fig. 4.9a is dramatically affected upon Ti adsorption. Figure 4.21c shows the electronic band structure and band-decomposed charge density analysis of the new structure in Fig. 4.21a. Each band consists of one spin-up and one spin-down state, which are located on different regions of the superlattice. The flat bands around Fermi level corresponds to confined states. The first valence band (V1) and second conduction band (C2) have their charge densities mostly confined in narrow regions of the superlattice. First conduction (C1) and second valence (V2) bands are d-states of titanium. The fifth valence band states (V5) propagate throughout the superlattice.

4.5 Conclusions

We reviewed two routes for functionalization of GNRs, which are superlattice formation through width modulation and adding modifying magnetic properties through TM atom doping. Various types of quantum structures made by size modulation of graphene-based nanoribbons are examined. The confinement of spin-unpolarized and spin-polarized electron and hole states can lead to interesting effects such as resonant tunneling and spin confinement. Variation of the bandgaps, confined state energies, and the strength of confinement with the width and length and composition of the constituent nanoribbons are the key features for future applications. Also, the variations in electronic and magnetic properties upon TM atom adsorption are analyzed depending on the adsorbate concentration, adsorption site, and the species of the adsorbent. We show that it is possible to obtain half-metallic GNRs through TM atom adsorption.

Appendix A: Details of density functional theory calculations

In calculating the electronic and magnetic properties using density functional theory [29], projector augmented wave (PAW) [47] approach within a PW91 [48]-GGA [49] approximation for the exchange and correlation functional is used as currently implemented in the VASP [50] software. Geometry optimizations are performed by allowing all atomic positions to vary; for bulk structures all cell parameters are optimized as well. The atomic positions are optimized by the conjugate gradient method, and the system is considered to be at equilibrium when Hellman–Feynman forces are below 10 me V/A. Monkhorst–Pack meshes with sufficient number of k-points are used to converge the energies. For 1D and 2D structures, the minimum size of the implemented k-point meshes are (21,1,1) and (11,11,1), respectively. Periodic boundary conditions are implemented in all directions, where sufficiently large vacuum (minimum of 10 Å) is inserted in directions without crystal symmetry to prevent artificial interactions. The kinetic energy cutoff for the plane wave basis set is chosen as $\hbar^2|k + G|^2/2m = 500$ eV when using PAW potentials and 350 eV

when using ultrasoft pseudopotentials. The convergence criterion for electronic relaxations has been set to 10^{-5} eV for all cases. The binding energies of TM atoms are calculated as $E_b = E[\text{graphene}] + E[\text{TM}] - E[(\text{graphene} + \text{TM})]$ in terms of the total energies of the host cell, $E[\text{graphene}]$, the free TM atom in its ground state $E[\text{TM}]$, and one TM atom adsorbed on a host cell, $E[\text{graphene}] + E[\text{TM}]$. Total energies are calculated in the same supercells keeping other parameters of the calculations fixed.

References

1. K.S. Novoselov, A.K. Geim, S.V. Morozov, D. Yiang, Y. Zhang, S.V. Dubonos, I.V. Grigorieva, A.A. Firsov, Science **306**, 666 (2004)
2. L.D. Landau, E.M. Lifshitz, *Statistical Physics,* 3rd edn. (Pergamon, Oxford, 1980)
3. R.E. Peirls, Helv. Phys. Acta **7**, 81 (1934)
4. N.D. Mermin, Phys. Rev. **176**, 250 (1968)
5. S. Cahangirov, M. Topsakal, E. Akturk, H. Sahin, Salim Ciraci, unpublished (arXiv:0811.4412)
6. M. Topsakal, E. Akturk, S. Ciraci, Phys. Rev. B **79**, 115442 (2009)
7. M.I. Katsnelson, K.S. Novoselov, A.K. Geim, Nat. Phys. **2**, 620 (2006)
8. A.K. Geim, K.S. Novoselov, Nat. Mater. **6**, 183 (2007)
9. K.S. Novoselov, A.K. Geim, S.V. Morozov, D. Jiang, M.I. Katsnelson, I.V. Grigorieva, S.V. Dubonos, A.A. Firsov, Nature **438**, 197 (2005); Y. Zhang, Y.-W. Tan, H.L. Stormer, P. Kim, Nature **438**, 201 (2005)
10. C. Ataca, E. Aktiirk, S. Ciraci, H. Ustunel, Appl. Phys. Lett. **93**, 043123 (2008)
11. C. Ataca, E. Akturk, S. Ciraci, Phys. Rev. B **79**, 041406 (2009)
12. F. Schedin, A.K. Geim, S.V. Morozov, E.W. Hill, P. Blake, M.I. Katsnelson, K.S. Novoselov, Nat. Mater. **6**, 652 (2007)
13. T.B. Martins, R.H. Miwa, A.J.R. da Silva, A. Fazzio, Phys. Rev. Lett. **98**, 196803 (2007)
14. M. Topsakal, H. Sevincli, S. Ciraci, Appl. Phys. Lett. **92**, 173118 (2008)
15. H. Sahin, R.T. Senger, Phys. Rev. B **78**, 205423 (2008)
16. Y.-W. Son, M. L. Cohen, S.G. Louie, Nature **444**, 347 (2006) (see also erratum: Nature **446**, 342 (2007))
17. Y.-W. Son, M.L. Cohen, S.G. Louie, Phys. Rev. Lett. **97**, 216803 (2006) (see also erratum: Phys. Rev. Lett. **98**, 089901(E) (2007))
18. J. Nilsson, A.H. Castro Neto, F. Guinea, N.M.R. Peres, Phys. Rev. B **76**, 165416 (2007)
19. X. Wang, Y. Ouyang, H. Wang, J. Guo, H. Dai, Phys. Rev. Lett. **100**, 206803 (2008)
20. H. Sevincli, M. Topsakal, S. Ciraci, Phys. Rev. B **78**, 245402 (2008)
21. C.H. Xu et al., J. Phys.: Condens. Matter **4**, 6047 (1992)
22. P.R. Wallace, Phys. Rev. **71**, 622 (1947)
23. G.W. Semenoff, Phys. Rev. Lett. **53**, 2449 (1984)
24. M. Fujita, K. Wakabayashi, K. Nakada, K. Kusakabe, J. Phys. Soc. Jpn. **65**, 1920 (1996)
25. L. Pisani, J.A. Chan, B. Montanari, N.M. Harrison, Phys. Rev. B **75**, 064418 (2007)
26. K. Nakada, M. Fujita, G. Dresselhaus, M.S. Dresselhaus, Phys. Rev. B **54**, 17954 (1996)
27. Y. Miyamoto, K. Nakada, M. Fujita, Phys. Rev. B **59**, 9858 (1999)
28. M. Ezawa, Phys. Rev. B **73**, 045432 (2006)
29. W. Kohn, L.J. Sham, Phys. Rev. **140**, A1133 (1965); P. Hohenberg, W. Kohn, Phys. Rev. B **76**, 6062 (1964)
30. E.H. Lieb, Phys. Rev. Lett. **62**, 1201 (1989)
31. L. Esaki, R. Tsu, IBM J. Res. Dev. **14**, 61 (1970)
32. L. Esaki, L.L. Chang, Phys. Rev. Lett. **33**, 495 (1974)

33. L. Esaki, *Highlights in Condensed Matter Physics and Future Prospects, NATO Advanced Studies Institute, Series B: Physics* (Plenum, New York, 1991), p. 285, several relevant references can be found in this proceedings; L.L. Chang, L. Esaki, R. Tsu, Appl. Phys. Lett. **24**, 593 (1974)

34. E. Tekman, S. Ciraci, Phys. Rev. B **40**, 8559 (1989); S. Ciraci, I. P. Batra, Phys. Rev. B **36**, 6194 (1987)

35. Claire Berger, Zhimin Song, Xuebin Li, Xiaosong Wu, Nate Brown, Cecile Naud, Didier Mayou, Tianbo Li, Joanna Hass, Alexei N. Marchenkov, Edward H. Conrad, Phillip N. First, Walt A. de Heer, Science **312**, 1191 (2006)

36. M.-Y. Han, B. Ozyilmaz, Y. Zhang, P. Kim, Phys. Rev. Lett. **98**, 206805 (2007)

37. B. (Ozyilmaz, P.J. -Herrero, D. Efetov, P. Kim, Appl. Phys. Lett. **91**, 192107 (2007)

38. R. Landauer, Philos. Mag. **21**, 863 (1970)

39. S. Datta, *Electronic Transport in Mesoscopic Systems* (Cambridge University Press, Cambridge, 1995)

40. M. Brandbyge, J.-L. Mozos, P. Ordejn, J. Taylor, K. Stokbro, Phys. Rev. B **65**, 165401, (2002)

41. D. Fisher, P. Lee, Phys. Rev. B **23**, 6851 (1981)

42. S. Tongay, R.T. Senger, S. Dag, S. Ciraci, Phys. Rev. Lett. **93**, 136404 (2004)

43. X. Li, X. Wang, L. Zhang, S. Lee, H. Dai, Science **319**, 1229 (2008)

44. J.F.-Rossier, J.J. Palacios, Phys. Rev. Lett. **99**, 177204 (2007)

45. L. Yang, C.-H. Park, Y.-W. Son, M.L. Cohen, S.G. Louie, Phys. Rev. Lett. **99**, 186801 (2007)

46. H. Sevincli, M. Topsakal, E. Durgun, S. Ciraci, Phys. Rev. B **77**, 195434 (2008)

47. P.E. Blochl, Phys. Rev. B **50**, 17953 (1994)

48. J.P. Perdew, J.A. Chevary, S.H. Vosko, K.A. Jackson, M.R. Pederson, D.J. Singh, C. Fiolhais, Phys. Rev. B **46**, 6671 (1992)

49. J.P. Perdew, K. Burke, M. Ernzerhof, Phys. Rev. Lett. **77**, 3865 (1996)

50. G. Kresse, J. Hafner, Phys. Rev. B **47**, 558 (1993); G. Kresse, J. Furthmuller, Phys. Rev. B **54**, 11169 (1996)